



Vortex-induced vibration of a cylinder in pulsating nanofluid flow

Y. Amini¹ · S. Akhavan² · E. Izadpanah¹

Received: 10 June 2019 / Accepted: 29 October 2019 / Published online: 6 November 2019
© Akadémiai Kiadó, Budapest, Hungary 2019

Abstract

In this paper, vortex-induced vibration of a circular cylinder with forced convection heat transfer and entropy generation in pulsating alumina–water nanofluid flow is investigated numerically. Numerical simulation is carried out for a constant mass ratio of 2 and damping ratio of 0.01 at a fixed Reynolds number of 150. The ranges of reduced velocity, particle volume fraction and inlet velocity oscillation amplitude are 3–8, 0–5% and 0–1, respectively. It was found that the lock-in phenomenon, nanofluid concentration and inlet velocity oscillation amplitude have an effective role in increasing heat transfer and decreasing entropy generation. Two wake patterns (2S and 2P) were observed in the present simulation. For velocity oscillation amplitude of 1, the transition from 2S to 2P modes occurs in vortex shedding pattern.

Keywords Vortex-induced vibration · Nanofluid · Pulsating flow · Entropy generation · Forced convection heat transfer

List of symbols

Be	Bejan number
C	Heat capacity (J Kg ⁻¹ k ⁻¹)
C_l	Lift coefficient
C_d	Drag coefficient
C_p	Heat capacity at constant pressure (J Kg ⁻¹ k ⁻¹)
D	Cylinder diameter (m)
d	Nanoparticle diameter (m)
f	Frequency (Hz)
h	Heat transfer coefficient (W/m ² K)
K	Thermal conductivity (W m ⁻¹ K ⁻¹)
K_b	Boltzmann constant (J k ⁻¹)
m	Mass (Kg)
Nu	Nusselt number
P	Pressure (Pa)
Pr	Prandtl number
q''	Heat transfer rate (W)
Rb	Kapitza resistance (K m ² W ⁻¹)
Re	Reynolds number
S'''	Entropy generation rate (J Kg ⁻¹ k ⁻¹)
St	Strouhal number
T	Temperature (K)
t	Time (s)

U	Free stream velocity (m s ⁻¹)
V	Fluid velocity (m s ⁻¹)
y	Cylinder vertical displacement (m)
Y	Nondimensional cylinder vertical displacement

Greek symbols

μ	Fluid viscosity (Pa s)
ρ	Density (Kg m ⁻³)
θ	Angular position (°)
α	Nanoparticle concentration (%)

Subscripts

bf	Base fluid
cyl	Cylinder
eff	Effective
eq	Equivalent
ff	Fluid friction
gen	Generated
ht	Heat transfer
loc	Local
n	Normalized
nf	Nanofluid
np	Nanoparticle
r	Reduced

✉ Y. Amini
Aminiyasser@pgu.ac.ir

¹ Department of Mechanical Engineering, Persian Gulf University, Bushehr 75169, Iran

² School of Mechanical Engineering, Tehran University, Tehran, Iran

Introduction

The vortex shedding phenomenon from a bluff body leads to oscillating forces which induce structural vibration. This phenomenon is known as vortex-induced vibration (VIV)

and can be found in a wide range of applications including nuclear reactors, heat exchangers, marine industry, bridges, buildings and chimneys. The VIV of a cylinder in cross-flow has been studied by researches in the past few decades due to its practical applications and importance in the design of structures [1]. Vortex shedding modes, oscillation amplitude branches (namely ‘initial,’ ‘upper’ and ‘lower’) and lock-in (the natural frequency of the cylinder is close to the vortex shedding frequency) are some subjects in the VIV which have been investigated [2]. The large amplitude of oscillations, significant increases in the drag and lift fluctuations and acoustic noise are the effects of VIV which can cause fatigue in the structures of offshore and wind turbines. Hence, various techniques have been presented to control and suppress VIV responses, which are classified as passive and active methods [3].

Most researches have been focused on the hydrodynamic characteristics of VIV [4], although the effects of cylinder vibration can be significant on the heat transfer characteristics, especially in lock-in or synchronization range [5–7]. The VIV of the cylinder can consider as a passive method in the heat transfer enhancement technology, unlike the pulsating flow is an active method. The effects of velocity oscillation frequency and amplitude, porosity and magnetic field in pulsating flow on heat transfer have been studied [5].

Adding nanoparticles (e.g., Al_2O_3 or CuO) to the base fluid (e.g., water, ethylene glycol and oil) is a passive method in the heat transfer enhancement technology [8–11]. This fluid suspension which is called nanofluid [12] is widely used in the thermal process to increase heat transfer due to their improved thermophysical properties [13–18]. The heat transfer and the viscous effect cause energy loss in any thermofluidic systems, so it is essential to calculate entropy generation to determine the irreversibilities. The entropy generation minimization (EGM) approach is used to optimizing thermofluidic systems and decreasing the irreversibilities [13–16, 19].

Although there are many studies concerning the effect of using nanofluid [20–25], pulsating flow [26, 27] or both on heat transfer of stationary circular cylinder [28, 29], a few

types of research have been performed for the oscillating cylinder. In the present work, for the first time, the effects of the combination of passive (nanofluid and VIV) and active (pulsating flow) methods on convective heat transfer and entropy generation of the circular cylinder have been investigated which can be important in heat exchangers.

Problem description

In this work, the forced convection of pulsating nanofluid flow over an elastically mounted cylinder which is free to oscillate in cross-flow (y -axis) is studied numerically. The configuration sketch of flow over the cylinder with a rectangular computational domain is shown in Fig. 1. The overall size of the domain in the inline and the transverse directions is 30D and 20D, respectively. The center of the cylinder is placed at 10D upstream from the inlet boundary, 20D downstream from the outlet boundary and 10D from the lateral boundaries. The grid which is used to solve the problem is illustrated in Fig. 2.

Governing equations and numerical method

The nanofluid used in the present study is Al_2O_3 –water which consists of nanoparticles with an average size of 29 nm. The thermophysical properties (dynamic viscosity, thermal conductivity, specific heat capacity, density) of the base fluid and the nanoparticles which are used for the calculations are presented in Table 1.

The following assumptions for nanofluid are considered: The nanofluid is homogenous, thermal equilibrium (locally) exists between the two phases and dynamic viscosity, and thermal conductivity of the nanofluid is dependent on temperature [32]. The governing equations for unsteady, incompressible nanofluid consist of the continuity, the momentum and the energy equations. Thus, in vector form, the conservation equations in an arbitrary Lagrangian–Eulerian (ALE) frame [33] are expressed as:

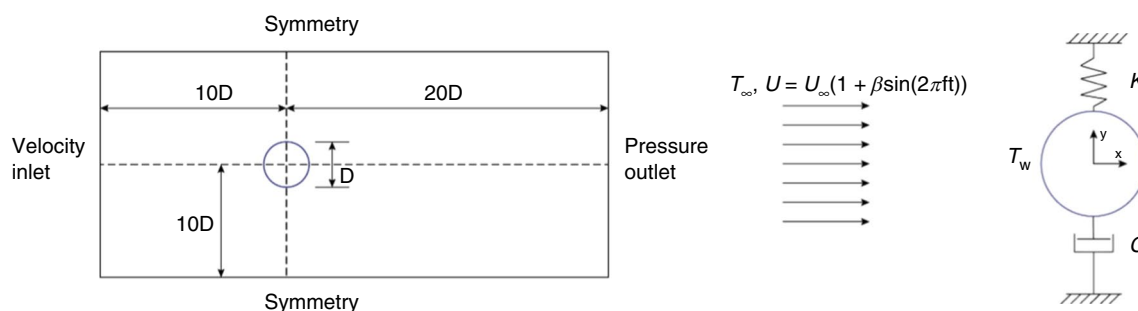


Fig. 1 Sketch of the circular cylinder: **a** computational domain and the boundary conditions **b** close-up view of a flexibly mounted cylinder

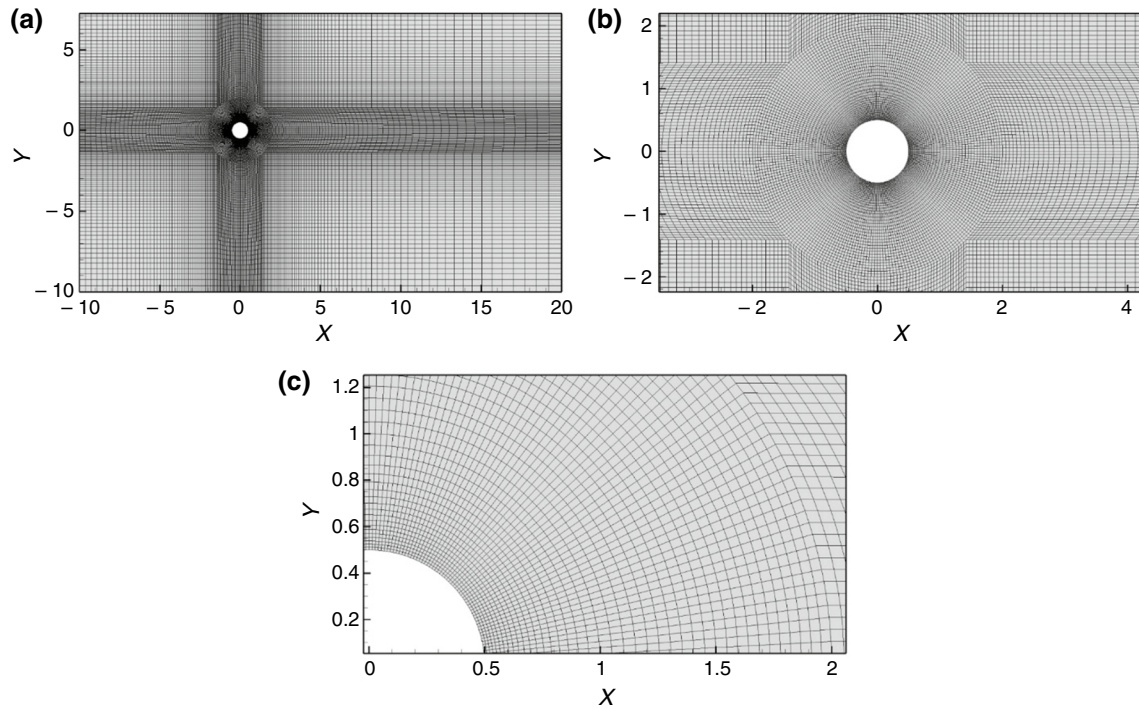


Fig. 2 Grid used to solve the problem

Table 1 Thermo-physical properties of Al₂O₃ nanoparticles and pure water

	Al ₂ O ₃ [30]	Pure water [31]
$\mu/\text{Pa s}$		$2.761 \times 10^{-6} \exp\left(\frac{1713}{T}\right)$
$K/\text{W m}^{-1} \text{K}^{-1}$	36	$0.6(1 + 4.167 \times 10^{-5}T)$
$C_p/\text{J kg}^{-1} \text{K}^{-1}$	765	4180
$\rho/\text{Kg m}^{-3}$	3970	1000

$$\nabla \cdot \mathbf{V}_{\text{nf}} = 0 \tag{1}$$

$$\rho \left[\frac{\partial \mathbf{V}_{\text{nf}}}{\partial t} + \left((\mathbf{V}_{\text{nf}} - \hat{\mathbf{V}}) \cdot \nabla \right) \mathbf{V}_{\text{nf}} \right] = -\nabla P + \mu_{\text{nf}} \nabla^2 \mathbf{V}_{\text{nf}} \tag{2}$$

$$\rho_{\text{nf}} c_{\text{nf}} \left[\frac{\partial T_{\text{nf}}}{\partial t} + \left(\mathbf{V}_{\text{nf}} - \hat{\mathbf{V}} \right) \cdot \nabla T_{\text{nf}} \right] = \nabla \cdot (k_{\text{nf}} \nabla T_{\text{nf}}) \tag{3}$$

where ρ, \mathbf{V}, P and μ are the density, velocity, pressure and dynamic viscosity of the fluid, respectively. Furthermore, T and k are the temperature and fluid conductivity, respectively. Subscript nf stands for the nanofluid. Also $\hat{\mathbf{V}}$ is the velocity of the mesh movement in y direction. The local

Nusselt number on the cylinder which depends on the angular position (θ) and time (t) is determined as follows:

$$\text{Nu}_{\text{loc}}(\theta, t) = \frac{h(\theta, t)D}{k_{\text{bf}}} \tag{4}$$

where k_{bf} is the base fluid thermal conductivity. $h(\theta, t)$ is the convective heat transfer coefficient on the cylinder surface and calculated as follows:

$$h = \frac{q''(\theta, t)}{T_w - T_\infty} \tag{5}$$

where $q''(\theta, t)$ is the heat flux from the cylinder surface. By integrating the local Nusselt number on the cylinder surface, the surface-average Nusselt number is obtained:

$$\text{Nu}(t) = \frac{1}{2\pi} \int_0^{2\pi} \text{Nu}_{\text{loc}}(\theta, t) dS \tag{6}$$

The time-average of Nusselt number can be calculated by integrating the surface-average Nusselt number in a period of cylinder's displacement (τ):

$$\overline{\text{Nu}} = \frac{1}{\tau} \int_0^\tau \text{Nu}(t) dt \tag{7}$$

Total entropy generation in a two-dimensional problem is evaluated as follows:

$$S'''_{gen} = \frac{k}{T^2} \left[\left(\frac{\partial T}{\partial X} \right)^2 + \left(\frac{\partial T}{\partial Y} \right)^2 \right] + \frac{\mu}{T} \left\{ 2 \left[\left(\frac{\partial u}{\partial X} \right)^2 + \left(\frac{\partial v}{\partial Y} \right)^2 \right] + \left(\frac{\partial u}{\partial Y} + \frac{\partial v}{\partial X} \right)^2 \right\} \tag{8}$$

The first term in the right-hand side of Eq. 9 is the entropy generation due to the heat transfer ($S'''_{g,ht}$), and the second term is the entropy generation due to the fluid friction ($S'''_{g,ff}$). Furthermore, to assess the contribution of the heat transfer and the fluid friction in total irreversibility, a non-dimensional parameter, the Bejan number (Be), is defined as follows [14]:

$$S_n = S'''_{gen} \frac{kT_{in}^2}{q''_{cyl}} \tag{9}$$

$$S_{n,ff} = S'''_{g,ff} \frac{kT_{in}^2}{q''_{cyl}} \tag{10}$$

$$S_{n,ht} = S'''_{g,ht} \frac{kT_{in}^2}{q''_{cyl}} \tag{11}$$

$$Be = \frac{S'''_{g,ht}}{S'''_{gen}} \tag{12}$$

By using the mixture model [34], the density of nanofluid is obtained as follows:

$$\rho_{nf} = (1 - \alpha)\rho_{bf} + \alpha\rho_{np} \tag{13}$$

where α is the volume fraction of nanoparticles. Subscripts nf, bf and np denote the nanofluid, the base fluid and the nanoparticle, respectively. The thermal conductivity of nanofluid is assumed as the combination of two parts [35]:

$$k_{nf} = k_{static} + k_{brownian} \tag{14}$$

Hamilton–Crosser model [36] is used to estimate k_{static} and $k_{brownian}$:

$$k_{static} = k_{bf} \left[\frac{(k_{np,eff} + 2k_{bf}) - 2\alpha(k_{bf} - k_{np,eff})}{(k_{np,eff} + 2k_{bf}) - \alpha(k_{bf} - k_{np,eff})} \right] \tag{15}$$

$$k_{brownian} = 5 \times 10^4 \alpha C_{p,bf} \rho_{bf} \sqrt{\frac{k_b T}{d_{np} \rho_{np}}} g(T, \alpha, d_{np}) \tag{16}$$

where k_b is the Boltzmann constant and equals to $1.3806503 \times 10^{-23} \frac{J}{k}$. The term $k_{np,eff}$ accounts for the effects of interfacial thermal resistance and is calculated as follows:

$$k_{np,eff} = \frac{d_{np}}{R_b + \left(\frac{d_{np}}{k_{np}} \right)} \tag{17}$$

where R_b is the Kapitza resistance ($4 \times 10^{-8} \frac{km^2}{W}$). Similar to Eq. 15, the effective viscosity is obtained as follows:

$$\mu_{nf} = \mu_{static} + \mu_{brownian} \tag{18}$$

$$\mu_{static} = \frac{\mu_{bf}}{(1 - \alpha)^{\frac{5}{2}}} \tag{19}$$

$$\mu_{brownian} = 5 \times 10^4 \alpha \rho_{bf} \sqrt{\frac{k_b T}{d_{np} \rho_{np}}} g(T, \alpha, d_{np}) \tag{20}$$

The function g is a semi-empirical relation for water- Al_2O_3 nanofluid and determined as follows [37]:

$$g = \left[(a + b \ln(d_{np}) + c \ln(\alpha) + d \ln(\alpha) \ln(d_{np}) + e \ln(d_{np})^2) \right] \ln(T) + [m + h \ln(d_{np}) + i \ln(\alpha) + j \ln(\alpha) \ln(d_{np}) + k \ln(d_{np})^2] \tag{21}$$

where the coefficients $a-k$ are listed in Table 2.

The cylinder displacement in the cross-flow is calculated by using a mass–spring–damping system as follows:

$$m_{eq} \ddot{y} + C_{eq} \dot{y} + k_{eq} y = f_l(t) \tag{22}$$

where y , \dot{y} and \ddot{y} are the displacement, velocity and acceleration of the cylinder in the cross-flow direction, respectively. $f_l(t)$ is the time-dependent lift force on the cylinder. The non-dimensional form of governing equation for the oscillating cylinder is expressed as:

$$\frac{d^2 y^*}{dt^{*2}} + \left(\frac{4\pi\zeta}{V_r} \right) \frac{dy^*}{dt^*} + \left(\frac{4\pi^2}{V_r^2} \right) y^* = \frac{C_L}{2m_r} \tag{23}$$

Table 2 Constant parameters of Eq. 22

Coefficient values	Water- Al_2O_3
<i>a</i>	52.813
<i>b</i>	6.116
<i>c</i>	0.696
<i>d</i>	4.175e-02
<i>e</i>	0.177
<i>m</i>	-298.198
<i>h</i>	-34.533
<i>i</i>	-3.923
<i>j</i>	-0.235
<i>k</i>	-0.999

where $V_r = U_\infty / (f_n D)$ is the reduced velocity, $f_n = (2\pi)^{-1} \sqrt{k_{eq} / m_{eq}}$ is the structural natural frequency of the cylinder, $m_r = m_{eq} / (\rho D^2)$ is the mass ratio, $\zeta = C_{eq} / (2\sqrt{m_{eq} k_{eq}})$ is the damping ratio and $C_L = f_L(t) / \frac{1}{2} \rho U_\infty^2 D$ is the lift coefficient.

In this work, the governing equations with the arbitrary Lagrangian–Eulerian frame are solved by using the finite volume method (commercial software FLUENT). An improved fourth-order Runge–Kutta algorithm is employed to solve the cylinder displacement equation (Eq. 22). So, in order to determine the velocity and the displacement of the cylinder and the thermophysical properties of nanofluid, two user-defined functions (UDFs, programmed in C language) are embedded into the code. The PISO (pressure implicit with splitting of operator) algorithm for velocity–pressure coupling is used to calculate the coupling between the pressure and velocity fields. The second-order upwind scheme is implemented to discretize the momentum and energy convective terms. Convergence criteria are chosen to be 10^{-6} for velocity components, continuity and energy equations to achieve reliable results. The first-order implicit scheme is applied for time discretization. The non-dimensional time step is set to $U_\infty \Delta t / D = 0.002$, to ensure that the results are independent of the time step size and the requirement of Courant–Friedrichs–Lewy (CFL) number being smaller than one [38].

Grid independence study and validation

The grid independence study is conducted on four grids with different densities for the stationary cylinder at Reynolds number of 150 and air (with constant properties) as the fluid. The properties of air are evaluated at 350 k. Table 3 compares the calculated averaged Nusselt numbers and lift and drag coefficients for different grid sizes. The difference between the results of meshes with the size of 34,000 and 87,000 is less than 0.03%. Therefore, the mesh with 34,000 cells is selected because of less calculation time needed compared to the more refined grid.

To establish the validity of the numerical method and accuracy of VIV computations, different cases were studied. In the first validation test case, numerical simulation of flow over a stationary cylinder at $Re = 100$ and 200 was performed

Table 3 Grid size independence study

Grid size	\overline{Nu}	C_l	C_d
6000	6.527	± 0.529	1.390 ± 0.025
16,000	6.431	± 0.540	1.382 ± 0.018
34,000	6.401	± 0.533	1.364 ± 0.027
87,000	6.399	± 0.528	1.362 ± 0.027

Table 4 Comparison of the calculated results with those reported in the literature. $Re = 100$

	\overline{Nu}	St	$\overline{C_d}$	$\overline{C_l}$	Uncertainty/%
<i>Numerical studies</i>					
Present study	5.164	0.167	1.384	± 0.339	–
Izadpanah et al. [40]	5.159	0.169	1.373	± 0.339	–
Mahir et al. [41]	5.179	0.172	1.368	± 0.343	–
Liu et al. [42]	–	0.164	1.350	± 0.339	–
Equation 24	5.16	–	–	–	–
<i>Experimental studies</i>					
Williamson [43]	–	0.164	–	–	–
Norberg [44]	–	0.168	–	± 0.180 to ± 0.540	5
Triton [45]	–	–	1.250	–	1

(air as the fluid) and the lift and the drag coefficients (C_d, C_l), the Strouhal (St) number and the Nusselt number are compared with the numerical and experimental results obtained from other researchers. Also, the calculated Nusselt numbers are compared with the Churchill and Bernstein correlation [39] (Eq. 24). Good agreement between the numerical and the experimental results with current modeling is observed (Tables 4 and 5).

$$Nu = 0.3 + \frac{0.62 Re^{\frac{1}{2}} Pr^{\frac{1}{3}}}{\left[1 + \left(\frac{0.4}{Pr}\right)^{\frac{2}{3}}\right]^{\frac{1}{4}}} \left[1 + \left(\frac{Re}{282000}\right)^{\frac{5}{8}}\right]^{\frac{1}{4}} \quad (24)$$

In the second validation test case, the simulation is performed for the VIV of a cylinder with the convective heat transfer at $Re = 150$, $m_r = 2$ and $\zeta = 0$. Water at 300 k with constant properties is used as the fluid. The maximum amplitude of vibrations is compared with those reported by researchers in Fig. 3 and achieved good agreement. The average Nusselt number for different reduced velocities is compared with those by Izadpanah et al. [40] in Fig. 4. The agreement between the present results and other numerical results is excellent.

Results and discussion

In this section, a complete numerical result for the forced convection heat transfer and entropy generation of pulsating nanofluid flow past a vibrating circular cylinder is presented for $m_r = 2$ and $\zeta = 0.01$. The thermo-hydrodynamic characteristics are investigated in the range of $0 \leq \alpha \leq 5\%$, $3 \leq V_r \leq 8$ and $0 \leq \beta \leq 1$. This result section is divided

Table 5 Comparison of the calculated results with those reported in the literature. $Re = 200$

	\overline{Nu}	St	$\overline{C_d}$	$\overline{C_l}$	Uncertainty (%)
<i>Numerical studies</i>					
Present study	7.546	0.200	1.374	± 0.698	–
Izadpanah et al. [40]	7.452	0.200	1.336	± 0.700	–
Mahir et al. [41]	7.474	0.192	1.376	± 0.698	–
Liu et al. [42]	–	0.192	1.310	± 0.690	–
Equation 32	7.190	–	–	–	–
<i>Experimental studies</i>					
Williamson [43]	–	0.196	–	–	–
Norberg [44]	–	0.180–0.197	–	± 0.350 to ± 0.700	5

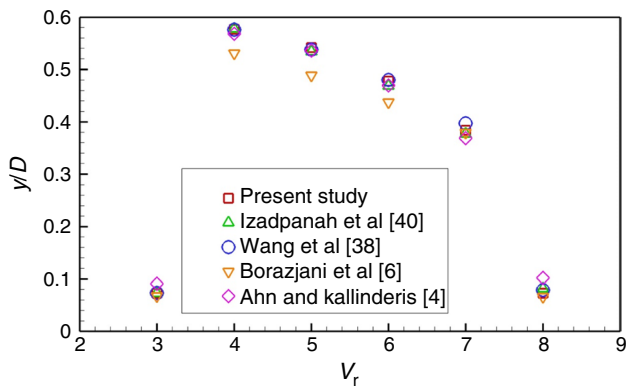


Fig. 3 Comparison of the cylinder displacement amplitude with the literature ($\zeta = 0$)

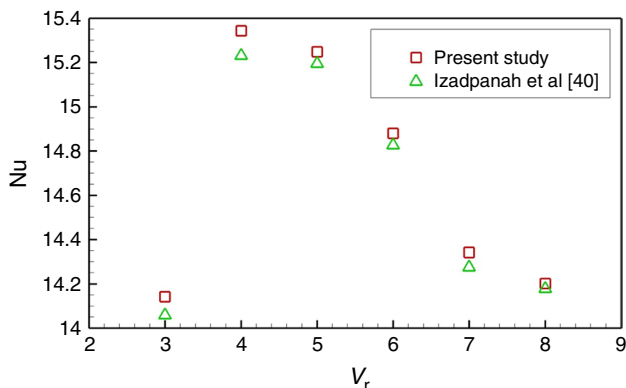


Fig. 4 Comparison of the Nusselt number with the literature ($\zeta = 0$)

into two subsections. The role of VIV (of nanofluid flow) on the heat transfer enhancement and entropy generation under the influence of constant inlet velocity is analyzed in ‘Vortex-induced vibrations of a cylinder: constant inlet velocity’ section and under pulsating inlet velocity in

‘Vortex-induced vibrations of a cylinder with oscillating inlet velocity’ section.

Vortex-induced vibrations of a cylinder: constant inlet velocity

Figure 5 shows time histories of lift coefficient, averaged Nusselt number and entropy generation on the cylinder for $\alpha = 5\%$ and $V_r = 4$. Furthermore, the vorticity contours of four different positions of the cylinder (namely a , b , c and d) are shown in this figure. As can be seen, the vortex shedding pattern is 2S (two single vortices shed per cycle) mode with two vortex streets. The vortices are shed in near maximum or minimum amplitude of cylinder displacement. The lift coefficient is in the same phase as the cylinder displacement. Since in one period of cylinder displacement two periods of Nusselt number (or entropy generation) occurred, the frequency of Nusselt number is two times of cylinder displacement. The time history of Nusselt number is similar to that of the entropy generation with the same frequency.

Figure 6 illustrates time histories of Nusselt number, entropy generation, their fast Fourier transform (FFT) analysis and corresponding vorticity contours for $V_r = 3 - 8$ and $\alpha = 5\%$. The vorticity contours are captured when the cylinder is located in its maximum position. The vortex shedding pattern for all reduced velocities is 2S mode with one or two vortex streets. The amplitude of cylinder displacement, Nusselt number and entropy generation is considerable for reduced velocities of 4–7, and the dominant frequency ratio of displacement (f/f_0) is close to one in these reduced velocities, so these reduced velocities are in the lock-in region. In the FFT analysis of Nusselt number and entropy generation at $V_r = 4$, two dominant frequencies are observed. Each of them is related to one of the two pikes which are existed in a period of Nusselt number or entropy generation.

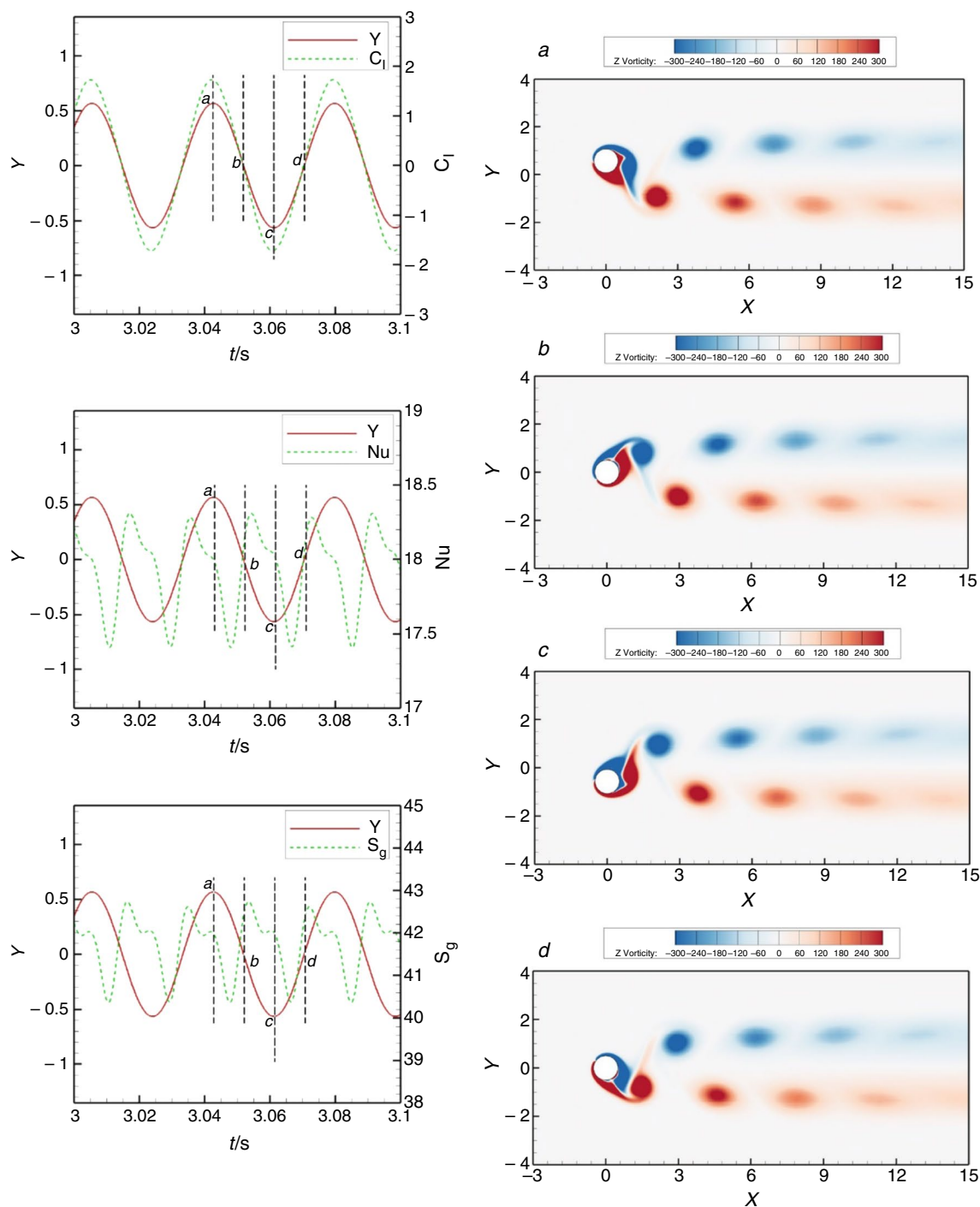


Fig. 5 Lift coefficient, Nusselt number and total entropy generation for different positions of the cylinder in a period of vibrations

The local entropy generation and the Nusselt number on the maximum position of the cylinder are illustrated in Fig. 7. These plots show that the maximum entropy generation and Nusselt number are related to the stagnation point of the cylinder. The local entropy generation and the Nusselt

number decrease continuously from the stagnation point to the boundary layer separation point. Moreover, because of flow mixing due to vortex forming and shedding, these two values increase in the rear of the cylinder. Figure 8 depicts the effects of the nanoparticle concentration on the local

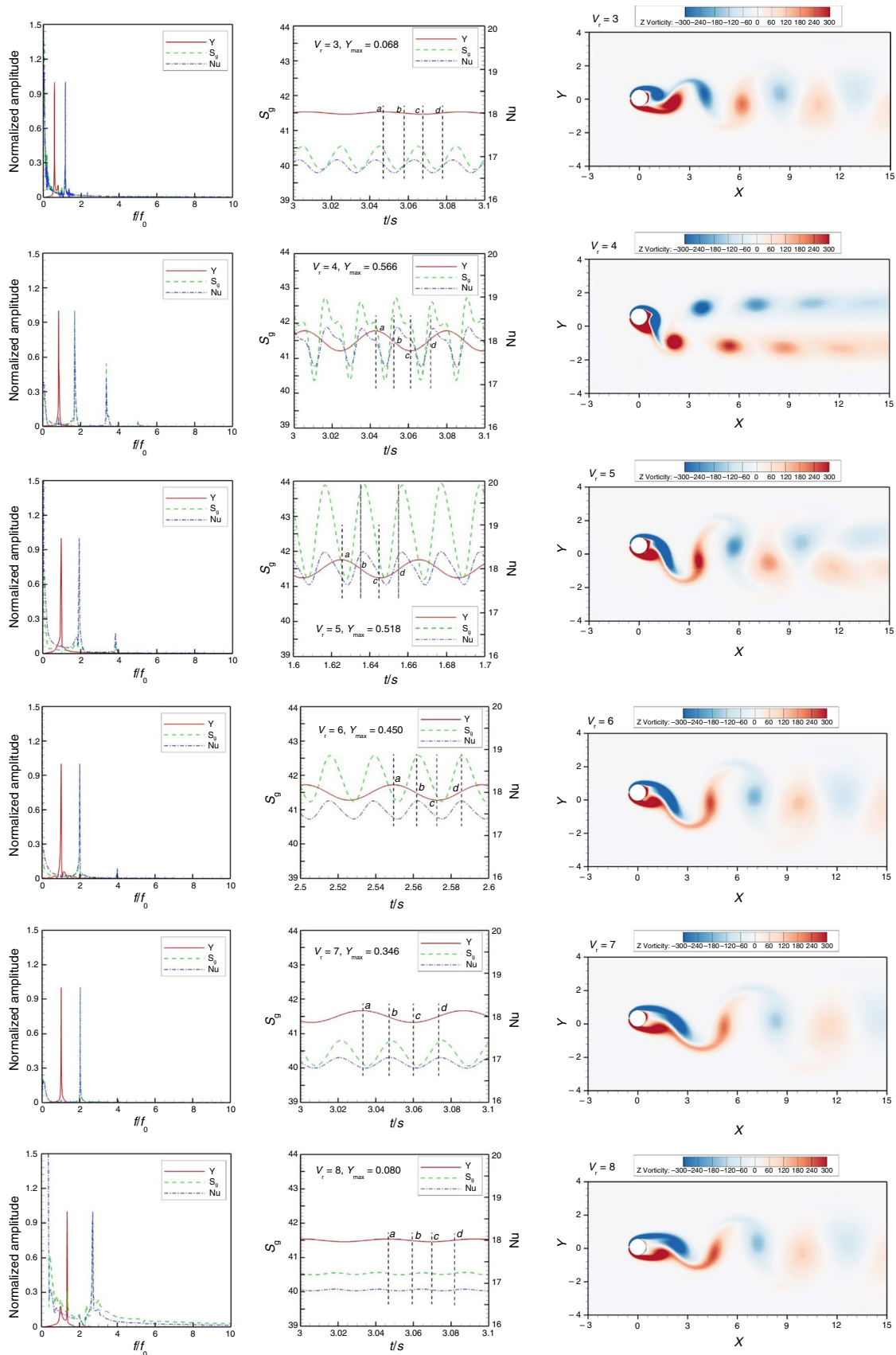


Fig. 6 Displacement, Nusselt number and total entropy generation for different reduced velocities of the cylinder

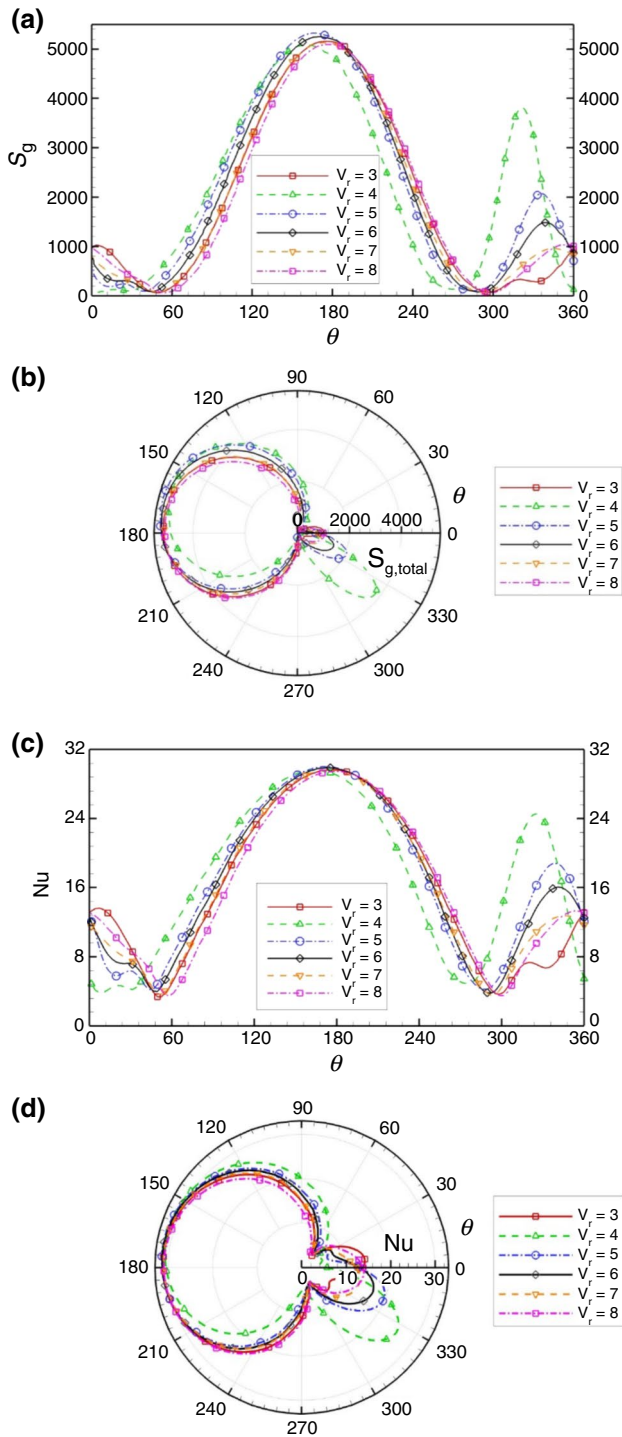


Fig. 7 Local entropy generation and Nusselt number plots when the cylinder is located at its maximum position, the results are plotted for different reduced velocities

entropy generation and Nusselt number. As can be seen, by increasing the nanoparticle concentration, the local Nusselt number increases. The maximum local Nusselt number increases by 19% in comparison with the pure water.

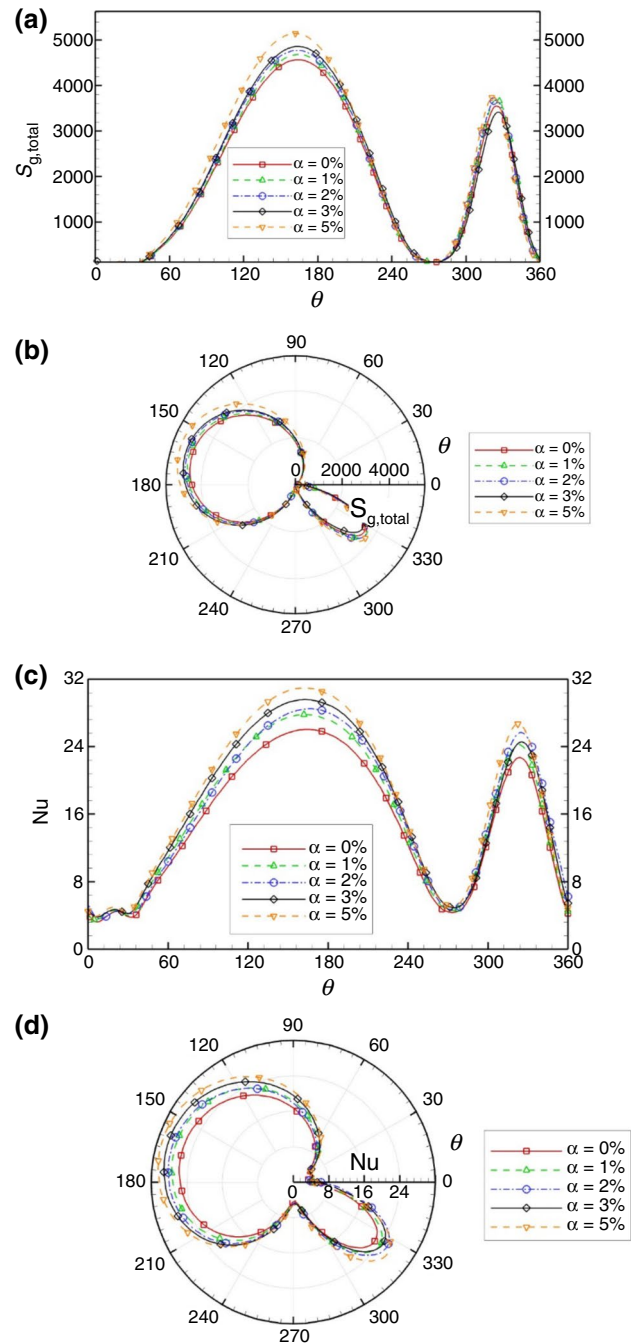


Fig. 8 Local entropy generation and Nusselt number plots when the cylinder is located at its maximum position, the results are plotted for different nanoparticle concentrations

The variation in averaged Nusselt number (\overline{Nu}), the total non-dimensional entropy generation ($S_{n,total}$) and Bejan number (Be) versus the reduced velocity for different values of the nanoparticle volume fraction (α) are shown in Fig. 9. By increasing the nanoparticle concentration, the fluid thermal conductivity increases, and consequently, the

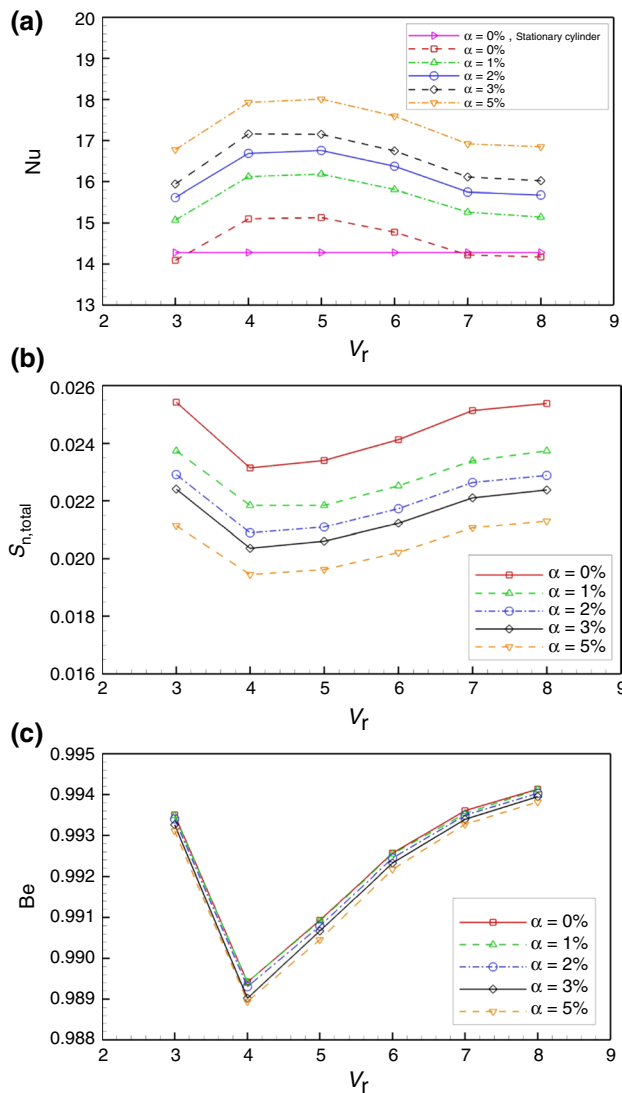


Fig. 9 Average Nusselt number, total non-dimensional entropy generation and Bejan number for different reduced velocities and nanofluid concentrations

heat transfer rate from the cylinder enhances. It is worth noting that when the induced lift force frequency is synchronized with the natural frequency of the system (a definition that was introduced by Sarpkaya [46]), the heat transfer rate from the cylinder surface increases compared to the stationary cylinder. Thus, at $\alpha = 5\%$ and $V_r = 4$ and 5 the Nusselt number reaches to its maximum because of higher nanoparticle volume fraction and maximum displacement amplitude. According to this figure, the maximum heat transfer enhancement with respect to the stationary cylinder is 26.1%. Moreover, for $V_r = 3, 7$ and 8 , the average Nusselt number is smaller than the fixed cylinder Nusselt number.

These results clearly show that the lock-in phenomenon can highly affect the heat transfer from a vibrating cylinder by means of different vortex shedding patterns and frequencies. By increasing the volume fraction of nanoparticles (α), the total non-dimensional entropy generation ($S_{n,total}$) decreases. For $V_r = 4$ and 5 , $S_{n,total}$ is minimum because of better heat transfer performance from the cylinder surface. Based on the results of these figures, synchronization can profoundly affect the entropy generation in the domain. Furthermore, using nanofluid with $\alpha = 5\%$ can decrease $S_{n,total}$ by 21% which leads to a significant reduction in the irreversibility produced by the heat transfer and the fluid friction. In analyzing the entropy generation, the Bejan number indicates the fraction of thermal entropy generation compared to the total entropy generation. As can be seen in Fig. 9c, by increasing α , the Bejan number decreases due to the heat transfer enhancement. Thus, the minimum and the maximum of Bejan number are related to $V_r = 4, \alpha = 5$ (with the maximum heat transfer rate from the cylinder) and $V_r = 8, \alpha = 0$ (with the minimum heat transfer rate from the cylinder), respectively.

There are two sources of entropy generation, e.g., due to fluid friction and heat transfer. Because the Bejan number is greater than 0.5 (≈ 1), the entropy generation due to the fluid friction can be neglected compared to the latter. Hence, Fig. 10 illustrates the contours of the entropy generation due to heat transfer in the domain. As can be seen from these figures, the entropy generation distribution in the domain is very similar to the vortex pattern of the cylinder. And this is because the temperature gradients are higher in the vortexes due to mixing the fluid in these regions.

Vortex-induced vibrations of a cylinder with oscillating inlet velocity

In this part of the study, the effects of harmonic inlet velocity with different frequencies and amplitudes on displacement, heat transfer and entropy generation of the cylinder are studied. Implemented harmonic inlet velocity is described as follows [47]:

$$U_{(t)} = U_{\infty}(1 + \beta \sin 2\pi ft) \quad (25)$$

The inlet velocity consists of two parts: a constant part (U_{∞}) and a harmonic part. The constant part is used for calculating Reynolds number and reduced velocity. The harmonic part causes inlet velocity oscillations, and its average is equal to zero in a period of inlet velocity oscillations. Constant β controls the inlet velocity oscillation amplitude, and the inlet velocity is constant for $\beta = 0$. Furthermore, f and t are the frequency of oscillations and time (s). Simulation

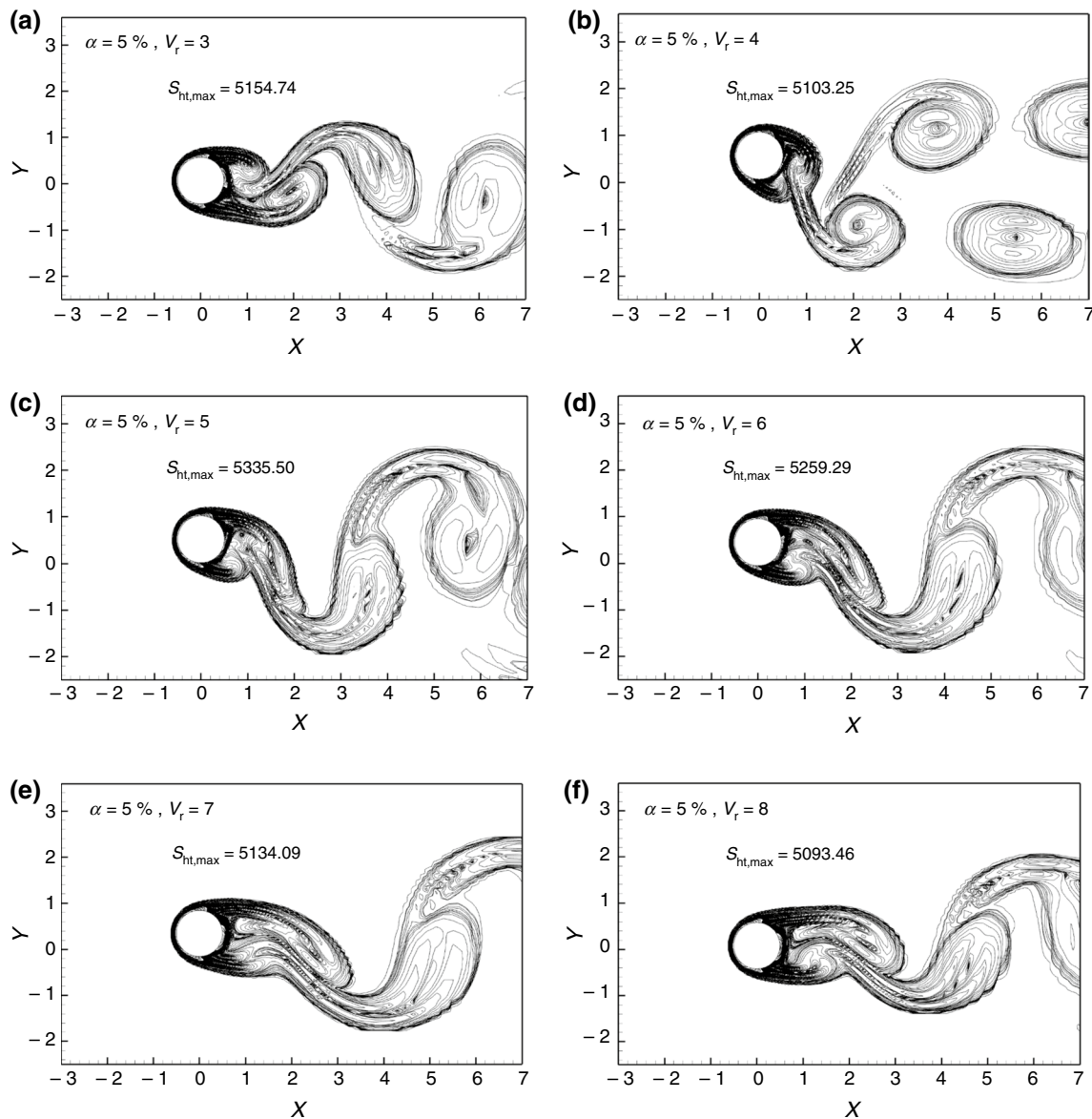


Fig. 10 Entropy generation contours in the domain due to heat transfer

is performed for reduced velocities of 4 and 6. The natural frequency of the system for these reduced velocities is 31 and 21 Hz, respectively. The inlet velocity frequency is set equal to these two natural frequencies.

Figure 11 depicts the vorticity contours of the cylinder for different inlet velocity oscillation amplitudes at $V_r = 4$ and 6. As can be observed, the vortex shedding pattern for $\beta = 0, 0.01, 0.10,$ and 0.25 at both reduced velocities is 2S mode with one or two vortex streets, whereas for $\beta = 1$, two pairs of vortices are shed from the cylinder (at two vortex streets) in one cycle of vibration (2P mode). Each pair of vortices contains the strong (first one) and weak (second

one) vortices. The second vortex disappears due to the friction in downstream.

Figure 12 shows time histories of the averaged Nusselt number, entropy generation, the cylinder displacement and their FFT analyses for different β at $V_r = 4$. The maximum variation in Nusselt number and entropy generation occurs at $\beta = 1$, although in this inlet velocity oscillation amplitude the cylinder displacement amplitude is lower than other β . In other words, at $\beta = 1$ the variation in heat transfer increases and the vibration of cylinder suppresses. There are two dominant frequencies in FFT analysis of $\beta = 1$, which are related to two extremum points in a period of cylinder displacement

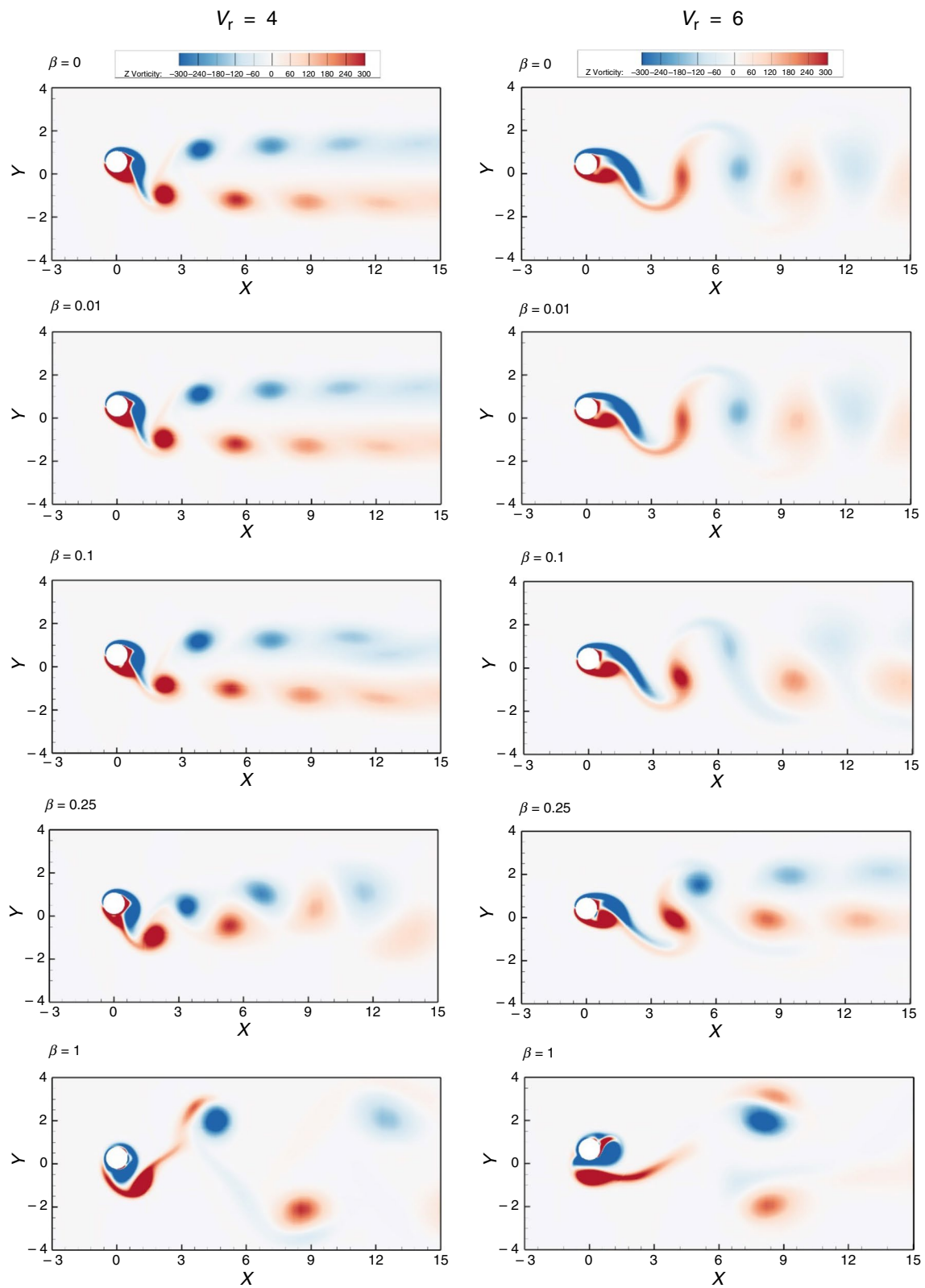


Fig. 11 Vortex shedding pattern of the cylinder for different values of the parameter β

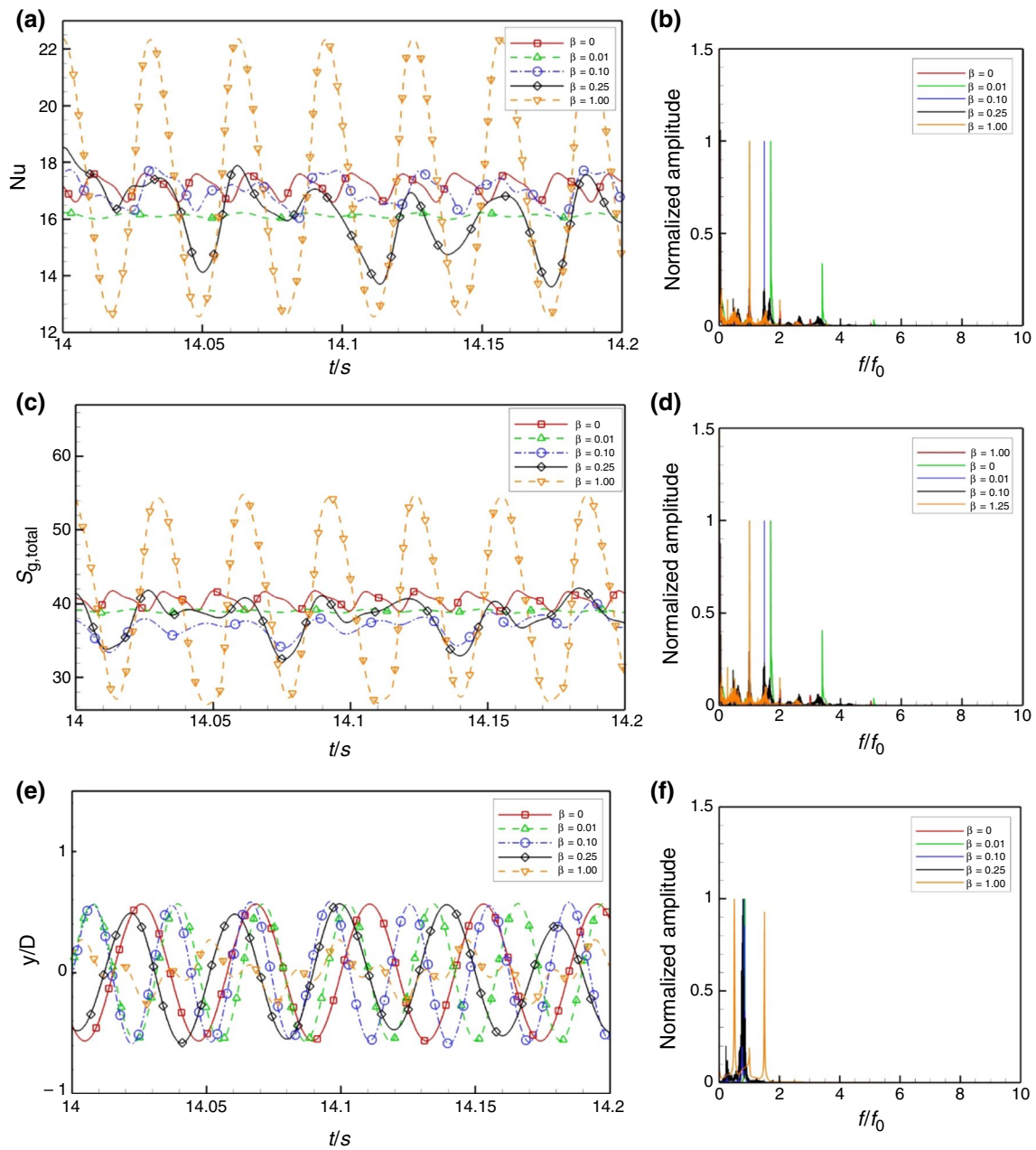


Fig. 12 Nusselt number, total entropy generation and non-dimensional displacement of the cylinder and their FFT for $V_r = 4$

and are due to the vortex shedding pattern (2P mode). The FFT analyses indicate that the dominant frequency of each of the three parameters can be significantly affected by the values of β .

Figure 13 illustrates time histories of the averaged Nusselt number, the entropy generation, the cylinder displacement and their FFT analyses for different β at $V_r = 6$. Unlike

$V_r = 4$, in this reduced velocity the variations in inlet velocity oscillation amplitude have not considerable effects on the cylinder displacement; also the dominant frequency of displacement at all β is close to one. But, like $V_r = 4$, the maximum variation in the Nusselt number and the entropy generation are related to $\beta = 1$.

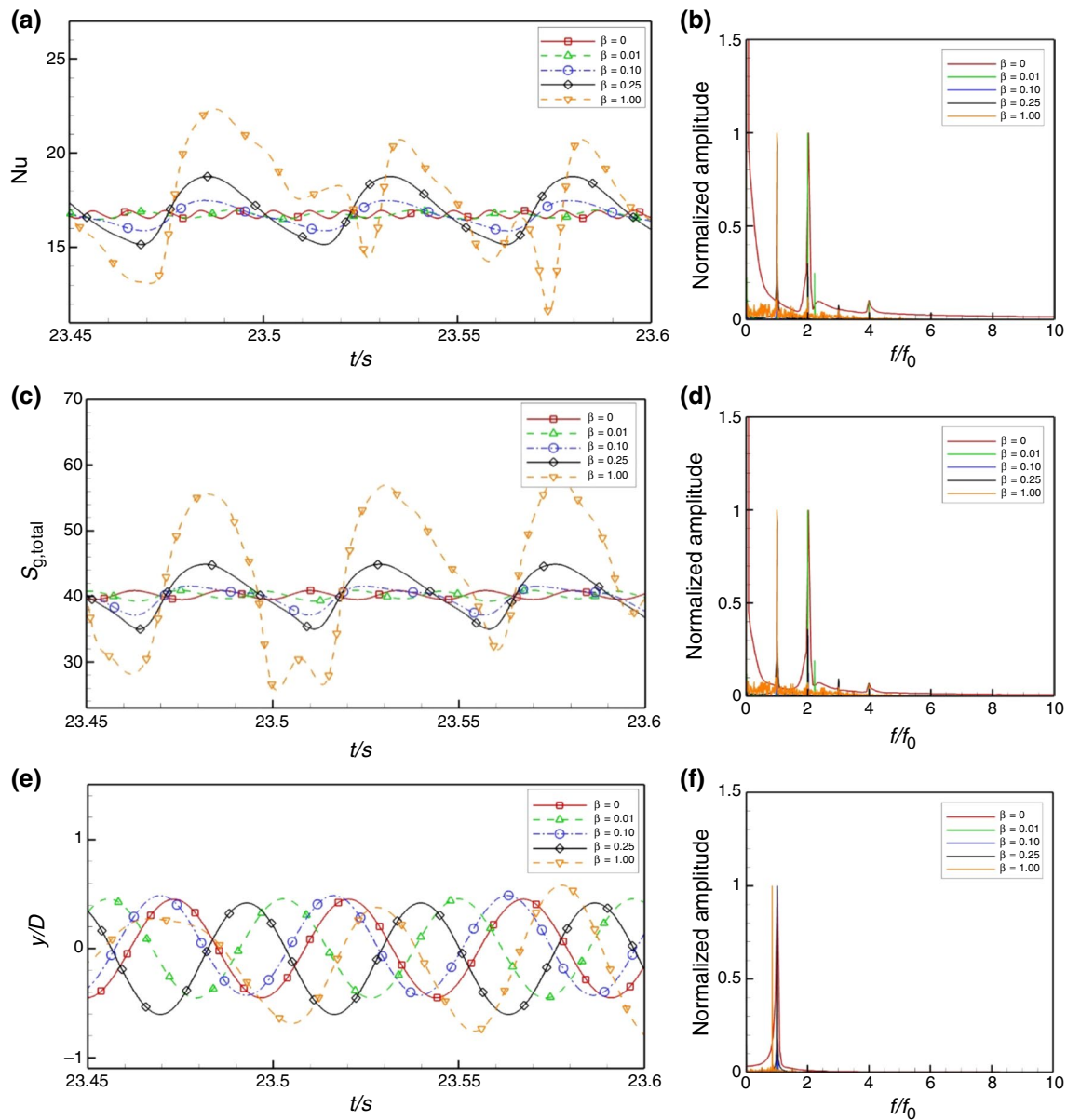


Fig. 13 Nusselt number, total entropy generation and non-dimensional displacement of the cylinder and their FFT for $V_i = 6$

Conclusions

Forced convection heat transfer and entropy generation of $\text{Al}_2\text{O}_3\text{-H}_2\text{O}$ nanofluid flow past a vibrating circular cylinder using a mass–spring–damping system were investigated. To evaluate the irreversibilities produced by the heat transfer and the friction, the entropy generation in the domain was evaluated. It was found that by increasing nanoparticle concentrations up to 5%, heat transfer from the cylinder can be enhanced by 26.1% compared to heat transfer from a fixed cylinder (pure water as fluid). In the lock-in region, both the average Nusselt number and the maximum amplitude of the cylinder displacement increased considerably. The entropy

generation due to heat transfer was dominant, and it can be investigated by inspecting Fig. 7c (where $Be \approx 1$). Furthermore, it was shown that by using nanofluid with $\alpha = 5\%$, the non-dimensional entropy generation can be reduced by 21% in the domain. To investigate the effects of free stream velocity oscillations on the cylinder displacement, the heat transfer, and the entropy generation, a harmonic part was added to it. By increasing the inlet velocity oscillation amplitude, the vortex shedding pattern changes from 2S to 2P. The inlet velocity oscillation amplitude had considerable effects on the variations in heat transfer, entropy generation and cylinder displacement (especially at $\beta = 1$).

References

- Parkinson G. Mathematical models of flow-induced vibrations of bluff bodies. *Flow Induc Struct Vib*. 1974;1974:81–127.
- Govardhan R, Williamson C. Modes of vortex formation and frequency response of a freely vibrating cylinder. *J Fluid Mech*. 2000;420:85–130.
- Carini M, Pralits J, Luchini P. Feedback control of vortex shedding using a full-order optimal compensator. *J Fluids Struct*. 2015;53:15–25.
- Ahn HT, Kallinderis Y. Strongly coupled flow/structure interactions with a geometrically conservative ALE scheme on general hybrid meshes. *J Comput Phys*. 2006;219(2):671–96.
- Cheng C-H, Hong J-L, Aung W. Numerical prediction of lock-on effect on convective heat transfer from a transversely oscillating circular cylinder. *Int J Heat Mass Transf*. 1997;40(8):1825–34.
- Borazjani I, Sotiropoulos F. Vortex-induced vibrations of two cylinders in tandem arrangement in the proximity-wake interference region. *J Fluid Mech*. 2009;621:321–64.
- Izadpanah E, Ashouri A, Liravi M, Amini Y. Effect of vortex-induced vibration of finned cylinders on heat transfer enhancement. *Phys Fluids*. 2019;31(7):073604.
- Sheikholeslami M. Magnetic field influence on CuO–H₂O nanofluid convective flow in a permeable cavity considering various shapes for nanoparticles. *Int J Hydrogen Energy*. 2017;42(31):19611–21.
- Sheikholeslami M. Numerical simulation for solidification in a LHTESS by means of nano-enhanced PCM. *J Taiwan Inst Chem Eng*. 2018;86:25–41.
- Sheikholeslami M. New computational approach for exergy and entropy analysis of nanofluid under the impact of Lorentz force through a porous media. *Comput Methods Appl Mech Eng*. 2019;344:319–33.
- Sheikholeslami M. Numerical approach for MHD Al₂O₃-water nanofluid transportation inside a permeable medium using innovative computer method. *Comput Methods Appl Mech Eng*. 2019;344:306–18.
- Mahian O, Kolsi L, Amani M, Estellé P, Ahmadi G, Kleinstreuer C, Marshall JS, Siavashi M, Taylor RA, Niazmand H. Recent advances in modeling and simulation of nanofluid flows-part I: fundamental and theory, Physics reports, (2018).
- Saeed M, Kim M-H. Heat transfer enhancement using nanofluids (Al₂O₃-H₂O) in mini-channel heatsinks. *Int J Heat Mass Transf*. 2018;120:671–82.
- Ebrahimi A, Rikhtegar F, Sabaghan A, Roohi E. Heat transfer and entropy generation in a microchannel with longitudinal vortex generators using nanofluids. *Energy*. 2016;101:190–201.
- Anbumeenakshi C, Thansekhar M. On the effectiveness of a nanofluid cooled microchannel heat sink under non-uniform heating condition. *Appl Therm Eng*. 2017;113:1437–43.
- Zhao Q, Xu H, Tao L. Nanofluid flow and heat transfer in a microchannel with interfacial electrokinetic effects. *Int J Heat Mass Transf*. 2018;124:158–67.
- Amini Y, Akhavan S, Izadpanah E. A numerical investigation on the heat transfer characteristics of nanofluid flow in a three-dimensional microchannel with harmonic rotating vortex generators. *J Therm Anal Calorim*. 2019. <https://doi.org/10.1007/s10973-019-08402-6>.
- Mahian O, Kolsi L, Amani M, Estellé P, Ahmadi G, Kleinstreuer C, Marshall JS, Taylor RA, Abu-Nada E, Rashidi S. Recent advances in modeling and simulation of nanofluid flows-part II: applications, Physics reports, (2018).
- Rashidi S, Akbarzadeh M, Karimi N, Masoodi R. Combined effects of nanofluid and transverse twisted-baffles on the flow structures, heat transfer and irreversibilities inside a square duct—a numerical study. *Appl Therm Eng*. 2018;130:135–48.
- Naderi B, Mohammadzadeh K. Numerical unsteady simulation of nanofluid flow over a heated angular oscillating circular cylinder. *J Therm Anal Calorim*. 2019. <https://doi.org/10.1007/s10973-019-08349-8>.
- Mehryan SAM, Izadpanahi E, Ghalambaz M, Chamkha A. Mixed convection flow caused by an oscillating cylinder in a square cavity filled with Cu–Al₂O₃/water hybrid nanofluid. *J Therm Anal Calorim*. 2019;137:965. <https://doi.org/10.1007/s10973-019-08012-2>.
- Mousavi SB, Heyhat MM. Numerical study of heat transfer enhancement from a heated circular cylinder by using nanofluid and transverse oscillation. *J Therm Anal Calorim*. 2019;135(2):935–45.
- Maskeen MM, Zeeshan A, Mehmood OU, Hassan M. Heat transfer enhancement in hydromagnetic alumina–copper/water hybrid nanofluid flow over a stretching cylinder. *J Therm Anal Calorim*. 1–10.
- Rashidi S, Kashеfi MH, Kim KC, Samimi-Abianeh O. Potentials of porous materials for energy management in heat exchangers—a comprehensive review. *Appl Energy*. 2019;243:206–32.
- Rashidi S, Eskandarian M, Mahian O, Poncet S. Combination of nanofluid and inserts for heat transfer enhancement. *J Therm Anal Calorim*. 2019;135(1):437–60.
- Fowler T IV, Witherden F, Girimaji S. Pulsating flow past a square cylinder at low Reynolds number: analysis of vortex structures. College Park: Bulletin of the American Physical Society; 2019.
- Srivastava A, Dhiman A. Pulsatile flow and heat transfer of shear-thinning power-law fluids over a confined semi-circular cylinder. *Eur Phys J Plus*. 2019;134(4):144.
- Hadad Y, Jafarpur K. Laminar forced convection heat transfer from isothermal bodies with unity aspect ratio in coaxial air flow. *Heat Transf Eng*. 2012;33(3):245–54.
- Hadad Y, Jafarpur K. Laminar forced convection heat transfer from isothermal cylinders with active ends and different aspect ratios in axial air flows. *Heat Mass Transf*. 2011;47(1):59–68.
- Bergman TL, Incropera FP, DeWitt DP, Lavine AS. Fundamentals of heat and mass transfer. Hoboken: Wiley; 2011.
- Yue Y, Mohammadian SK, Zhang Y. Analysis of performances of a manifold microchannel heat sink with nanofluids. *Int J Therm Sci*. 2015;89:305–13.
- Xuan Y, Roetzel W. Conceptions for heat transfer correlation of nanofluids. *Int J Heat Mass Transf*. 2000;43(19):3701–7.
- A. Bejan, Convection heat transfer, John Wiley & sons, 2013.
- Pak BC, Cho YI. Hydrodynamic and heat transfer study of dispersed fluids with submicron metallic oxide particles. *Exp Heat Transf Int J*. 1998;11(2):151–70.
- Koo J, Kleinstreuer C. A new thermal conductivity model for nanofluids. *J Nanopart Res*. 2004;6(6):577–88.
- Hamilton R, Crosser O. Thermal conductivity of heterogeneous two-component systems. *Ind Eng Chem Fundam*. 1962;1(3):187–91.
- Li J. Computational analysis of nanofluid flow in microchannels with applications to micro-heat sinks and bio-MEMS (2008).
- Wang C, Tang H, Duan F, Simon C. Control of wakes and vortex-induced vibrations of a single circular cylinder using synthetic jets. *J Fluids Struct*. 2016;60:160–79.
- Churchill S, Bernstein M. A correlating equation for forced convection from gases and liquids to a circular cylinder in crossflow. *J Heat Transf*. 1977;99(2):300–6.
- Izadpanah E, Amini Y, Ashouri A. A comprehensive investigation of vortex induced vibration effects on the heat transfer from a circular cylinder. *Int J Therm Sci*. 2018;125:405–18.

41. Mahir N, Altaç Z. Numerical investigation of convective heat transfer in unsteady flow past two cylinders in tandem arrangements. *Int J Heat Fluid Flow*. 2008;29(5):1309–18.
42. Liu C, Zheng X, Sung C. Preconditioned multigrid methods for unsteady incompressible flows. *J Comput Phys*. 1998;139(1):35–57.
43. Williamson C. 2-D and 3-D aspects of the wake of a cylinder, and their relation to wake computations. *Lect Appl Math Am Math Soc*. 1991;28:719.
44. Norberg C. Fluctuating lift on a circular cylinder: review and new measurements. *J Fluids Struct*. 2003;17(1):57–96.
45. Tritton DJ. Experiments on the flow past a circular cylinder at low Reynolds numbers. *J Fluid Mech*. 1959;6(4):547–67.
46. Sarpkaya T. Hydrodynamic damping, flow-induced oscillations, and biharmonic response. *J Offshore Mech Arct Eng*. 1995;117(4):232–8.
47. Andraka C, Diller T. Heat-transfer distribution around a cylinder in pulsating crossflow. *J Eng Gas Turbines Power*. 1985;107(4):976–82.

Publisher's Note Springer Nature remains neutral with regard to jurisdictional claims in published maps and institutional affiliations.